Mesoscopic Cluster Lifetime Informs the Transition Timescale in Clogging Probability Models

Zemin Qiu[a,*]

[a]Southwest Jiaotong University, No.111, North 1st Section of Second Ring Road, ChengDu, 610031, SiChuan, China

ARTICLE INFO

Keywords:
suspensions
rheological
clusters lifetime
particles clogging model
LBM-IBM-DEM

ABSTRACT

This study investigates the rheological behavior and the dynamic evolution of particle clusters in non-Brownian suspensions under linear shear flow using high-fidelity fully resolved LBM-IBM-DEM simulations. The research aims to provide a direct physical basis for the key fitting parameter in probability-based clogging prediction models. We first validated the accuracy of our simulations at both the macroscopic (apparent viscosity) and microscopic (radial distribution function) scales, and analyzed the effects of shear rate and particle volume fraction on rheological properties. The results indicate that the apparent viscosity increases significantly with the particle Reynolds number and volume fraction. The radial distribution function reveals pronounced spatial correlations of particles along the compressional axis, consistent with the orientation of contact force chains. More importantly, using a self-developed cluster tracking algorithm, we discovered that cluster lifetimes follow an exponential distribution, and their normalized form is independent of cluster size—demonstrating that their evolution is governed by a universal stochastic process. This mesoscopic-scale finding indicates that the state transition rates in probability models can be scaled by a simple characteristic time, enhancing the model's physical interpretability and providing a new theoretical basis for accurately predicting the flow stability and clogging risk of suspensions.

1. Introduction

Suspensions are widely present in nature and engineering, and their flow stability is crucial. From geological landslides (Kamali Zarch, Zhang, Haeri and He (2025)) and drilling pipe sticking (Yang, Li, Li, Li, Kadhim Kadhim, Li, Duan and Li (2024)) to industrial transport (Li, Zhao, Li, Yin, Song and Hao (2026)), clogging is a common failure mode. Therefore, developing theoretical models capable of accurately predicting clogging risk holds significant scientific and engineering value.

Recently, Herale, Pearce and Hewitt (2025) proposed an analytical framework based on mixture theory from a macroscopic continuum perspective. Another effective approach is probability models at the particle scale, such as the

ZM.Chiu@my.swjtu.edu.cn (Z. Qiu)
ORCID(s): 0000-0002-8438-2661 (Z. Qiu)

random walk model proposed by To, Lai and Pak (2001), or static arch models based on Poisson processes (Zuriguel, Pugnaloni, Garcimartín and Maza (2003); Mankoc, Garcimartín, Zuriguel, Maza and Pugnaloni (2009)), Building on this, Zhang, Zeng, Yuan, Li and Wang (2024) proposed a probability model that divides particle clogging into two processes: the formation of particle chains and the evolution of chains into clogging arches. In gravity-driven clogging, the former is only related to geometry, while the latter is related to particle velocity. In our previous work (Qiu and Xiao (2025)), we further applied this model to analyze clogging in fluid-driven flows, finding that flow boundaries influence both of the two processes. However, a key dynamic parameter in this model (the integration time step for the chain-to-arch transition) relies on fitting results, which limits the mechanistic interpretability of the model. The root cause lies in our lack of quantitative understanding of the dynamic characteristics of clogging precursors—transient particle clusters.

The evolution of particle clusters serves as a mesoscopic bridge connecting microscopic interactions with macroscopic rheology and clogging probability. At the macroscopic scale, phenomenological relationships such as the effective viscosity of suspensions have been extensively studied (Einstein (1911, 1906); Krieger and Dougherty (1959)); at the microscopic scale, the radial distribution function reveals shear-induced anisotropic structures (Li, Guo, Yang and Zhao (2023); Guazzelli and Pouliquen (2018)). An insightful study comes from Nabizadeh, Singh and Jamali (2022), where the authors used a community detection algorithm to distinguish behaviors between continuous shear thickening (CST) and discontinuous shear thickening (DST) in suspensions, highlighting the value of cluster analysis. However, regarding the dynamic characteristics of the mesoscopic clusters themselves, especially how their "lifetime" distribution is influenced by flow conditions, our knowledge remains limited.

The core objective of this study is to provide direct observational support for the time step fitting parameter in the aforementioned probability model. Through high-fidelity fully resolved simulations using LBM-IBM-DEM, we quantify the dynamic evolution of non-Brownian particle clusters in shear flow, with a focus on their lifetime distribution. We first verify that the simulations are consistent with classical results at the macroscopic and microscopic scales, and analyze potential influencing factors in the simulations. Subsequently, using a self-developed cluster tracking algorithm, we reveal that cluster lifetimes follow an exponential distribution, and their normalized form is independent of cluster size—this proves they are governed by a universal stochastic process. This finding is crucial: it indicates that the state transition rates in probability models can be scaled by a simple, physically meaningful characteristic time.

2. Methodology

2.1. Experiments setup

Linear shear flow (Couette flow) is employed to simulate the shearing motion of the suspension. The simulation diagram is shown in Figure 1. The computational domain is $L = 500 \times 10^{-3}$ m long in the x-direction and $H = 256 \times 10^{-3}$ m high in the y-direction. The top and bottom walls move in opposite directions with speed magnitude U_w, while the left and right boundaries are periodic. The macroscopic shear rate is therefore $\dot{\gamma} = 2U_w/H$. Particles are mono-disperse and their radius r is characterised by the non-dimensional ratio $\delta = r/H$. Brownian, electromagnetic and other body forces are neglected. A power-law model is used to mimic both shear-thinning and shear-thickening continuous phases.

The particle Reynolds number is used to quantify the motion of particles in the fluid. For a Newtonian fluid it reads

$$Re_p = \frac{\dot{\gamma} r^2}{\nu} \tag{1}$$

For non-Newtonian fluids the viscosity varies with the local shear rate, so the above definition is no longer applicable. Instead, the homogenisation approach proposed by Chateau, Ovarlez and Trung (2010); Alghalibi, Lashgari, Brandt and Hormozi (2018) is adopted to estimate an effective particle Reynolds number. The mean local shear rate is defined as

$$\bar{\dot{\gamma}}_{\text{local}}(\phi) = \sqrt{\langle \dot{\gamma}_{\text{local}}(x,y) \rangle} = \dot{\gamma} \sqrt{\frac{G(\phi)}{1-\phi}} \tag{2}$$

with

$$G(\phi) = \left(1 + B \frac{\phi}{1 - \phi/\phi_c}\right)^2 \tag{3}$$

where the first equality in Eq.(2) can be evaluated directly from the simulation and the second equality is the corresponding theoretical estimate. $G(\phi)$ is the non-dimensional relative shear viscosity and depends only on the solid volume fraction ϕ. The fitting parameter B is about 1.25–1.5 (Ergun (1952)), and ϕ_c is the random-close-packing volume fraction. In this study we take $B = 1.5$ and $\phi_c = 0.64$.

The power-law viscosity is evaluated with the mean local shear rate:

$$\hat{\mu}(\bar{\dot{\gamma}}_{\text{local}}(\phi)) = \hat{m} \bar{\dot{\gamma}}^{n-1}_{\text{local}}(\phi) \tag{4}$$

Table 1
Model parameters for the linear shear flow

Parameter	Value
Geometry	
Domain size $l_x \times l_y$ (mm)	500×256
Grid resolution	
Number of lattices $N_x \times N_y$	500×256
Fluid properties and boundary conditions	
Kinematic viscosity ν_f ($m^2\ s^{-1}$)	5×10^{-5}–5×10^{-3}
Density ρ_f ($kg\ m^{-3}$)	1×10^3
Wall speed U_w ($m\ s^{-1}$)	5×10^{-2}
Particle volume fraction	0.07–0.54
Particle properties	
Size ratio $\delta = r/H$	30
Density ρ_s ($kg\ m^{-3}$)	3000
Size dispersity $r_{\max}/r_{\min}$	1
Contact parameters	
Friction coefficient μ	0.4
Effective modulus E^* ($N\ m^{-2}$)	1×10^6
Normal/tangential stiffness ratio κ^*	0.1
Normal critical damping β_n	0.1

and the local particle Reynolds number is then written as

$$Re_{p,\mathrm{local}} = \frac{\rho_f r^2 \dot{\gamma}}{\mu_f(\bar{\dot{\gamma}}_{\mathrm{local}})} \tag{5}$$

All test cases are restricted to $Re_p < 1$, and the particle volume fraction ϕ_v ranges from 7% to 54%. In addition, the Stokes number is kept small to guarantee a viscous-force-dominated regime. The complete parameter set is summarised in Table1.

2.2. LB-IB-DEM solver

Numerical simulations were conducted using the previously developed LBM-IBM-DEM coupled framework (Qiu and Xiao (2025)). Within this framework, the fluid fields (pressure and velocity) and the solid particles (motion and contact) are resolved by the Lattice Boltzmann Method (LBM) and the Discrete Element Method (DEM), respectively, with their coupling handled by the Immersed Boundary Method (IBM). As a fully resolved approach, it offers a key advantage over unresolved or semi-resolved methods: the direct resolution of flow details around particle surfaces.. The non-Newtonian fluid model and code validation are provided in Appendix A.

3. Apparent viscosity

Apparent viscosity is defined as the ratio of the shear stress exerted on the fluid to the resulting shear rate, and it serves as a measure of the fluid's ability to flow. For a suspension, the relative apparent viscosity is

$$\eta_r = \frac{\langle \tau \rangle}{\eta_l \dot{\gamma}} \tag{6}$$

where η_l is the viscosity of the suspending (liquid) phase and $\dot{\gamma}$ is the macroscopic shear rate. The average shear stress $\langle\tau\rangle$ is obtained from the mean shear rate at the wall, $\dot{\gamma}_{\text{local}}$, via

$$\tau = \eta_l \dot{\gamma}_{\text{local}} \tag{7}$$

Two approaches are available to estimate the local shear rate at the wall. The first is a finite-difference approximation:

$$\dot{\gamma}_{\text{local}} = \frac{U_w - U_{xw}}{\Delta y} \tag{8}$$

where U_w and U_{xw} are the stream-wise velocities of the wall node and its immediate neighbour, respectively, and $\Delta y = 0.5$ (in lattice units, in this study we use link-wise method to layout grid, if using wet-node method, $\Delta y = 1$. For more details, please refer to Krüger, Kusumaatmaja, Kuzmin, Shardt, Silva and Viggen (2016) section 5) is the spacing between the two nodes. The second approach evaluates the local shear rate directly from Eq.(A-3) at the wall lattice cells.

In comparative tests using linear shear flow, the finite-difference scheme (Eq. (8)) yields an error of 45% relative to the theoretical value, while the LBM-based formula (Eq. (A-3)) reduces the error to 8%. Due to the relatively large errors observed in these preliminary tests and the heightened sensitivity of gradient-based methods to grid resolution, the LBM direct-evaluation approach is adopted for all subsequent simulations.

3.1. Influence of Shear Rate

The rheological response was examined for several distinct initial particle configurations. Figure 1 gives a snapshot in the statistically stationary regime, showing the particle orientation distribution together with the fluid velocity field. To guarantee comparability among different shear rates, the non-dimensional time $t^* = \dot{\gamma}t$ is used to set the simulation length. Every 10 Lattice Time Steps (LTU) the local shear stress is sampled to monitor the evolution of the apparent viscosity.

The temporal evolution of the relative apparent viscosity obtained with Eq.(6) is displayed in Figure 2. The particle Reynolds number ranges from 0.01 to 0.57. Owing to persistent particle contacts and collisions the apparent viscosity exhibits pronounced oscillations. For the present Re_p interval the viscosity decreases monotonically with time and eventually reaches a steady plateau.

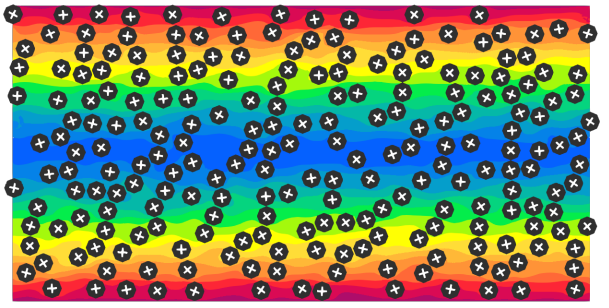

Figure 1: Snapshot of the sheared suspension at $t^* = 100$. White crosses indicate particle orientation; coloured contours show the velocity magnitude. $\phi_v = 39\%$, $Re_p = 0.03$.

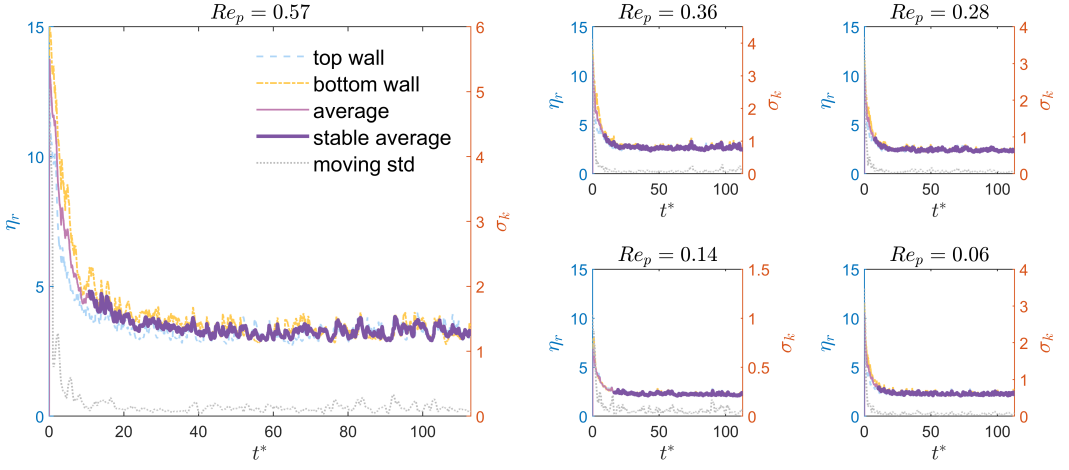

Figure 2: Apparent viscosity and its moving standard deviation versus time. Shear rate is fixed; Re_p is varied by changing the fluid viscosity ν. All curves start from the same initial particle configuration.

To quantify the approach to steady state, a moving standard deviation σ_k is introduced (grey dotted curves in Figure 2):

$$\sigma_k = \sqrt{\frac{1}{w-1} \sum_{i=k-w+1}^{k} (X_i - \mu_k)^2} \tag{9}$$

where w is the window size, X_i is the i-th datum inside the window, and $\mu_k = \frac{1}{w} \sum_{i=k-w+1}^{k} X_i$ is the window average. Here w is set to 200LTU. When σ_k falls below 2% of its maximum value the flow is considered statistically stationary (thick purple line in Figure 2). Because the viscosity still exhibits small fluctuations in the plateau region, the mean shear stress is averaged over the entire steady window to yield the final estimate $\bar{\eta}_r$, plotted in Figure 3.

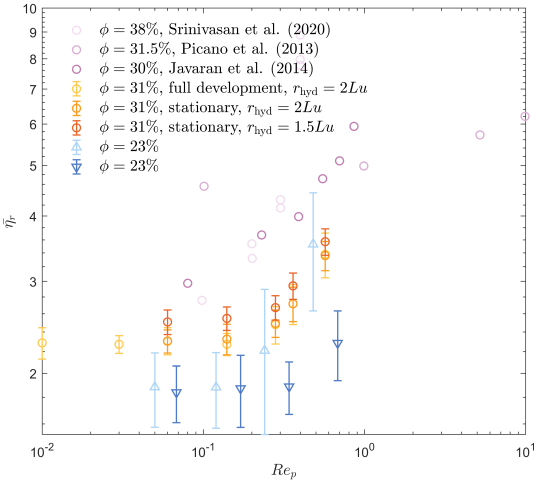

Figure 3: Steady-state apparent viscosity $\bar{\eta}_r$ versus particle Reynolds number. Unless stated otherwise, circles denote Newtonian fluid, upward triangles shear-thinning fluid, and downward triangles shear-thickening fluid.

Figure 3 shows that, regardless of the fluid model, the apparent viscosity increases with Re_p, a shear-thickening behaviour. For instance, when Re_p rises from 0.01 to 0.57 the viscosity of the Newtonian suspension grows by a factor of 1.47. The same trend has been reported previously, yet the absolute values differ considerably: at $Re_p \approx 0.36$ the present Newtonian result is 2.71, whereas Jahanshahi Javaran, Rahnama and Jafari (2014). obtain 3.98, Picano, Breugem, Mitra and Brandt (2012) interpolate 4.7, and Srinivasan, Van den Akker and Shardt (2020) et al. 6.9. The following discussion focuses on the origin of these discrepancies.

First, the influence of the initialisation strategy was examined. When the flow starts from a quiescent field the fluid must accelerate from rest to the target shear rate and the particles must evolve from a random configuration towards a dynamic equilibrium. A linear initial velocity profile may skip the cluster-formation stage and thus alter the viscosity history. In the present work the initial velocity is linear across the gap, whereas Sudharsan started from a stagnant field. The two approaches lead to very different convergence times: the present non-dimensional time to reach steady state is only 100, one quarter of theirs (the 2D/3D difference may also contribute). An additional test starting from a stagnant field (orange circle with error bar in Figure 3) yields a steady viscosity only 2% higher, confirming that 100 dimensionless time units are sufficient for the micro-structure to stabilise.

A second possible cause is the effective hydrodynamic radius. As discussed in Qiu and Xiao (2025), the radius seen by the LBM solver is reduced by $r_{\mathrm{hyd}} = 2\mathrm{Lu}$ to prevent numerical divergence. Consequences include an underestimated solid volume fraction (for $\delta = r/H = 30$ and a porosity of 0.6 the difference amounts to 58%), larger inter-particle gaps that diminish collisional dissipation, and an enlarged fluid domain. Srinivasan et al. (2020) adopted a much smaller

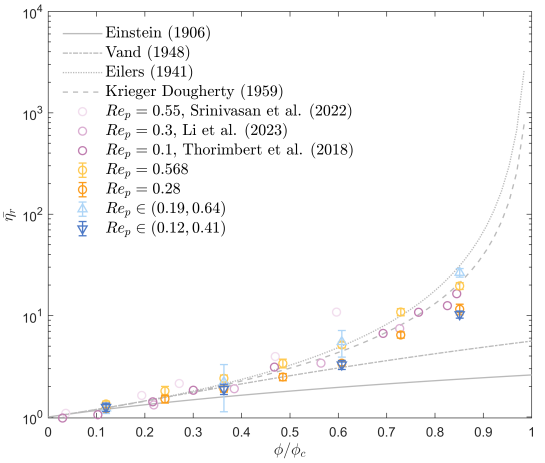

Figure 4: Steady-state apparent viscosity $\bar{\eta}_r$ versus particle volume fraction

reduction of 0.2Lu. A test with $r_{\text{hyd}} = 1.5$Lu (dark-orange symbol in Figure 3) shows a pronounced increase in apparent viscosity, demonstrating the sensitivity to the hydrodynamic radius.

Closely related is the choice of contact model. For numerical stability, Srinivasan et al. (2020); Jahanshahi Javaran et al. (2014) introduced a threshold-triggered short-range repulsion:

$$F_{\text{rep}} \propto \frac{1}{h - 2R - \epsilon} \tag{10}$$

where h is the gap between particle surfaces, R the radius, and ϵ the activation threshold. The repulsive force grows nonlinearly as the gap decreases, allowing momentary numerical overlap. An alternative remedy is the lubrication correction (Srinivasan, Akker and Shardt (2021)), which slows the relative approach through viscous resistance:

$$F_{\text{lub}} \propto \frac{U_n}{h} \tag{11}$$

with U_n the normal component of the relative velocity.

In summary, the detailed modelling of particle-scale interactions has a dominant influence on the estimated macroscopic viscosity, underscoring the controlling role of inter-particle forces in suspension rheology.

3.2. Effect of Particle Volume Concentration

Solid volume fraction is a key factor governing the apparent viscosity. Here ϕ is evaluated by accounting for both the DEM contact radius and the effective hydrodynamic radius used in the LBM solver:

$$\phi = \frac{\sum_p \pi \left[(r_{\mathrm{DEM}} + r_{\mathrm{LBM}})/2 \right]^2}{L_x L_y} \tag{12}$$

The investigated range is $7\% \le \phi \le 54\%$. To facilitate comparison, the data are plotted against the non-dimensional ratio ϕ/ϕ_c, with $\phi_c \approx 0.64$ for monodisperse disks. Figure 4 compares the simulation results with classical theoretical and semi-empirical expressions.

In the dilute regime ($\phi/\phi_c < 0.2$) the relative viscosity grows linearly with ϕ, as first described by the Einstein model (Einstein (1906, 1911), grey solid line in Figure 4):

$$\eta_r = 1 + B\phi, \qquad B = 2.5 \tag{13}$$

At higher concentrations particle interactions and collisions become non-negligible, giving rise to a nonlinear increase. Vand introduced a quadratic correction (Vand (1948), grey dash-dotted line):

$$\eta_r = 1 + 2.5\phi + 7.349\phi^2 \tag{14}$$

Alternative expressions include the Eilers equation (Eilers (1941), grey dotted line):

$$\eta_r = \left[1 + \frac{5/4\,\phi}{1 - \phi/\phi_c} \right]^2 \tag{15}$$

and the widely used Krieger–Dougherty formula (Krieger and Dougherty (1959), grey loosely-dotted line):

$$\eta_r = (1 - \phi/\phi_c)^{-B\phi_c} \tag{16}$$

Across the entire concentration range the present data agree well with Eq.(16), corroborating the accuracy of the numerical approach.

3.3. Particle Stress

The preceding sections have shown that the suspended particles govern the macroscopic rheology. To clarify how particle inertia and motion contribute to the total shear stress, the apparent viscosity is decomposed following

Batchelor's volume-averaged stress formulation (Batchelor (1970)):

$$\eta_r = \frac{\eta_{\text{apparent}}}{\eta_l} = \frac{\langle S_{xy} \rangle}{\eta_l \dot{\gamma}} \tag{17}$$

where $\langle S_{xy} \rangle$ is the suspension-averaged shear stress, consisting of a viscous contribution from the liquid and a particle-induced contribution:

$$S_{xy} = \eta_l \dot{\gamma} + S^p_{xy} \tag{18}$$

The particle stress S^p_{xy} is split into a hydrodynamic part S^{H}_{xy} and a contact part S^{C}_{xy}:

$$S^p_{xy} = n\langle S^{\mathrm{H}}_{xy} \rangle + n\langle S^{\mathrm{C}}_{xy} \rangle \tag{19}$$

with n the number density of particles and $\langle \cdot \rangle$ an ensemble average. The hydrodynamic stresslet is obtained from the surface traction exerted by the fluid:

$$S^{\mathrm{H}}_{xy} = \frac{1}{2} \int (\sigma_{ik} r_j + r_i \sigma_{jk}) \, \mathrm{d}A \tag{20}$$

where σ_{ik} is the fluid stress tensor. In practice the integral is discretised over the immersed-boundary (IB) markers:

$$S^{\mathrm{H}}_{xy} = \frac{1}{2} \sum \left(F^{\mathrm{IB}}_i r_j + r_i F^{\mathrm{IB}}_j \right) \tag{21}$$

with $\boldsymbol{F}^{\mathrm{IB}}$ the force on an IB node and $\boldsymbol{r}$ the vector from the particle centroid to that node. An analogous expression is used for the contact stresslet:

$$S^k_{ij} = \frac{1}{2} \sum \left(F_i r_j + r_i F_j \right) \tag{22}$$

where $\boldsymbol{F}$ is now the contact force and $\boldsymbol{r}$ the vector from the centroid to the contact point.

Figure 5 compares the two evaluation approaches. Instantaneous evolutions follow similar trends, but the difference grows markedly with ϕ: 20% at $\phi = 0.23$ and 50% at $\phi = 0.54$. The wall method reflects the local stress state near the boundary, whereas the bulk method captures the particle-induced stress over the entire domain. To illustrate the origin of the discrepancy, Figure 6 shows the vertical profiles of shear rate, fluid velocity and solid velocity, all normalised by the macroscopic shear rate and wall speed. As ϕ increases the velocities of both phases deviate from the reference single-phase profile. At high concentration ($\phi \approx 0.55$) particles in the centre are almost jammed; their translational

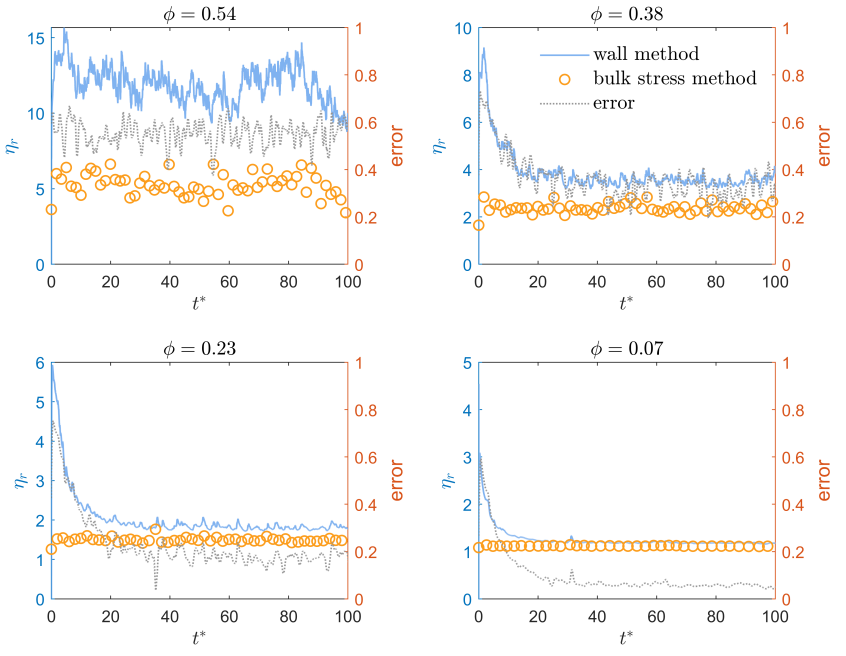

Figure 5: Comparison between wall-based (Eq.(6), lines) and bulk-stress-based (Eq.(17), symbols) relative viscosity at $Re_p = 0.28$

and rotational velocities approach zero, forcing the fluid into narrow wall layers (shear-banding(Boyer, Guazzelli and Pouliquen (2011))). Consequently the local shear rate near the wall rises sharply, and the wall-based estimate overshoots the domain-averaged value.

Figure 7 quantifies the respective contributions of contact and hydrodynamic stresses. The left column shows the influence of Re_p (or $Re_{p,\mathrm{local}}$ for non-Newtonian cases). Increasing the Reynolds number raises both contributions, but the contact fraction grows more slowly in the shear-thinning fluid because its viscosity decreases with shear rate, making stress transmission through direct contacts less efficient; hydrodynamic forces dominate instead.

The right column displays the effect of solid volume fraction. In the dilute regime the contact contribution is negligible. As ϕ increases, collisions and friction intensify and the contact term becomes dominant: at $\phi = 0.54$ it accounts for 71%, 67% and 68% of the total particle-induced viscosity for Newtonian, shear-thinning and shear-thickening fluids, respectively.

4. Particle Radial Distribution Function

To further clarify how inter-particle interactions affect the apparent viscosity, the statistical correlation of particle motion in shear flow is analysed by means of the radial distribution function. The radial distribution function $g(\boldsymbol{r})$ gives the probability density of finding a particle at position $\boldsymbol{r}$ relative to a reference particle, normalised by the uniform

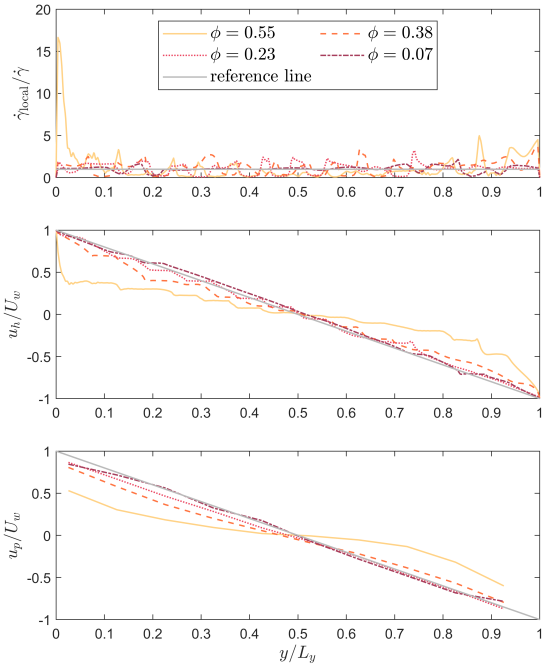

Figure 6: Profiles of shear rate, fluid stream-wise velocity and particle stream-wise velocity for a Newtonian suspension at $Re_p = 0.28$. Reference lines denote the single-phase theoretical values.

density:

$$g(\boldsymbol{r}) = \frac{\langle \rho(\boldsymbol{r}) \rangle}{\rho_0}$$

In two dimensions it is evaluated as

$$g(r_x, r_y) = \frac{1}{\rho_0} \left\langle \sum_{i<j} 2\delta(r_x - \Delta x_{ji}) \delta(r_y - \Delta y_{ji}) \right\rangle \tag{23}$$

where δ is the Dirac delta, $\rho_0 = (N/L_x L_y)^2$ is the areal number density of an ideal gas, and Δx_{ji}, Δy_{ji} are the components of the vector from particle i to particle j. Because the x-direction is periodic, the minimum-image convention is applied:

$$\Delta x_{\mathrm{mic}} = \Delta x_{ji} - \left\lfloor \frac{\Delta x_{ji}}{L_x} \right\rceil L_x \tag{24}$$

with $\lfloor \cdot \rceil$ denoting rounding to the nearest integer.

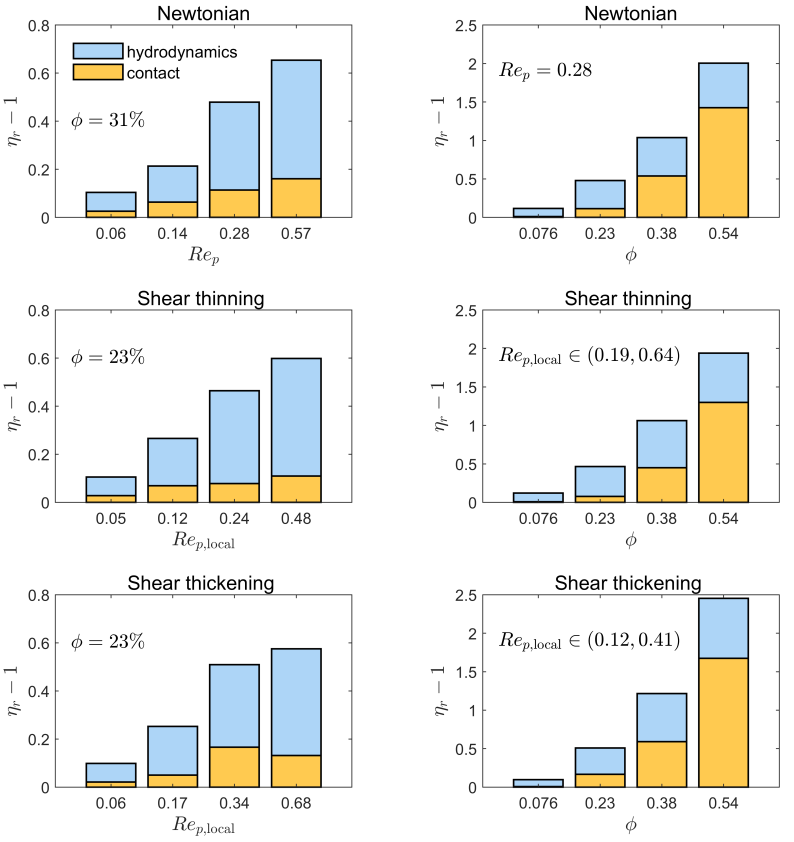

Figure 7: Relative apparent viscosity induced by particle stress for different fluid models

Results are shown in Figure 8 for volume fractions $\phi = 0.07, 0.23$ and 0.54 (left to right) and for Newtonian, shear-thinning and shear-thickening fluids (top to bottom). Distances are normalised by the particle radius, $r_x^* = r_x/r$, and the maps are binned with a resolution of $0.15r$. At low ϕ the distribution is almost featureless, indicating a nearly random structure. As ϕ increases, collision frequency rises and pronounced maxima appear in the lower-left and upper-right quadrants. The symmetric part of the rate-of-strain tensor is $\boldsymbol{E}^{\mathrm{sym}} = \frac{1}{2}\dot{\gamma}\begin{bmatrix} 0 & 1 \\ 1 & 0 \end{bmatrix}$, so the compressional axis is oriented at $\approx 45°$, in close alignment with the maxima of $g(\boldsymbol{r}^*)$. Figure 9 shows a snapshot of the force network at $\phi = 0.31$ and $Re_p = 0.57$; most active contacts (red rectangles) lie along the same diagonal direction. At the highest concentration the particles are almost locked into a lattice-like arrangement; consequently $g(\boldsymbol{r}^*)$ exhibits pronounced periodic peaks parallel to the flow and separated by one particle diameter.

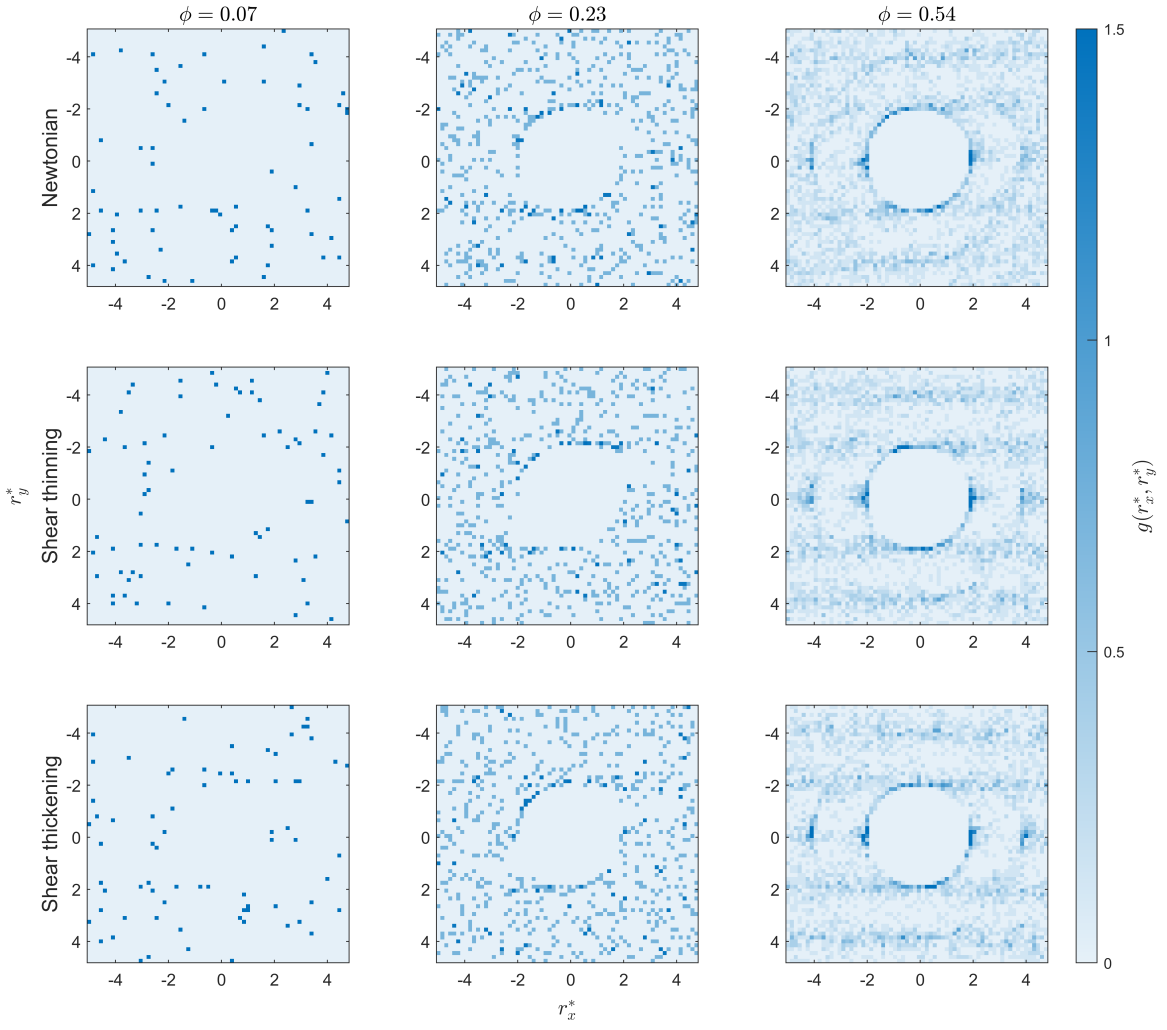

Figure 8: Two-dimensional radial distribution function $g(r_x^*, r_y^*)$

5. Cluster-Scale Behaviour Analysis

The foregoing analyses of the radial distribution function and the dominance of contact stress have highlighted the central role of inter-particle interactions in suspension rheology. To understand how these interactions organise and evolve during sustained shearing, and how they ultimately feed back on the macroscopic viscosity, we now examine the dynamics of mesoscopic particle agglomerates—clusters. This section quantifies cluster identification, evolutionary kinetics and lifetime characteristics, thereby bridging micro-scale interactions and the macro-rheological response.

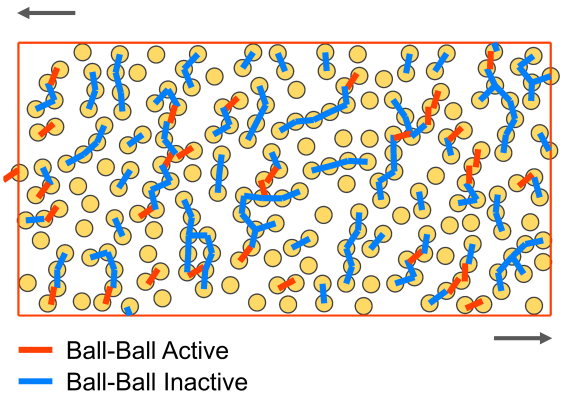

Figure 9: Morphology of particle contacts in linear shear flow. "Inactive" contacts are potential contacts detected during the contact-search phase; a contact is marked "active" only if the surfaces overlap. The inter-particle gap is defined as the centre-to-centre distance minus the sum of the two radii. $Re_p = 0.57$, $\phi = 0.31$.

5.1. Cluster Identification Algorithm

Clusters are defined as connected sets of particles linked by contacts (active or inactive) detected within the DEM stage. As illustrated in Figure 9, an inactive contact implies no force transmission, yet the particles are still hydrodynamically coupled and move cooperatively. Thus both active and inactive contacts are included when building the contact network.

Thøgersen, Dabrowski and Malthe-Sørenssen (2016) introduced a percolation threshold $\langle \epsilon_c \rangle$ that relates the critical contact gap to solid fraction:

$$\langle \epsilon_c \rangle = \left(1 - \frac{\phi}{\phi_c}\right)\left[\left(\frac{\phi}{\phi_c}\right)^{-0.5} - 1\right] \tag{25}$$

When $\phi \to \phi_c$ the threshold vanishes and system-spanning percolating clusters appear; for $\phi < 0.2$ the threshold is large and only small clusters exist. In the intermediate range ($\phi = 0.3$–0.5) $\langle \epsilon_c \rangle$ lies between 0.1 and 0.4, yielding non-percolating yet well-defined clusters whose size distribution and dynamics are amenable to statistical analysis. All subsequent investigations are therefore restricted to $0.3 \leq \phi \leq 0.5$.

Implementation is straightforward: every particle is visited once, and a recursive colouring algorithm labels all particles reachable through the contact list, producing a unique cluster ID for each connected aggregate.

Time resolution is crucial for frame-to-frame matching. If the interval is too large, significant split/merge events may be missed or clusters may travel farther than their own size, complicating tracking. If it is too small, collision-induced noise is recorded and the data set becomes unnecessarily large. Here the detection interval is chosen as the

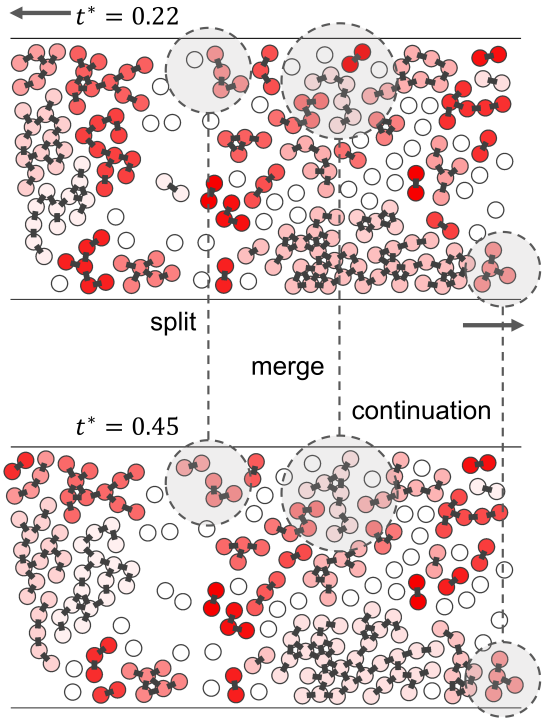

Figure 10: Types of cluster events: continuation, splitting, and merging. The color of particles distinguishes the number of clusters they belong to in a time slice. Black rectangles represent particle contacts.

time required for a particle to advect one diameter at the wall speed:

$$\Delta t_{\text{det}} = \frac{2r}{U_w} \approx 59\text{LTU} \tag{26}$$

In practice snapshots are stored every 50LTU.

After the time series is collected, clusters are matched between consecutive frames by exploiting the continuity of their core particle sets. Candidate pairs are first screened by requiring significant particle overlap ($> 85\%$). Among the remaining candidates the best match is selected according to positional and velocity similarity. Five distinct events are recognised and processed in the following order: continuation, splitting, merging, birth and death (Figure 10).

The continuation score S_c is defined as

$$S_c = \frac{n_o}{\min(n_{\Delta t}, n_{\Delta t+1})} \tag{27}$$

where n_o is the number of particles common to both frames. Continuation is accepted if $S_c > 0.85$. Splitting and merging are identified whenever the overlap exceeds one particle. All unmatched clusters are finally tagged as either newly born or extinct.

Once the inter-frame correspondence is established, a life-line is constructed for every physical cluster, and its lifetime is defined as the elapsed time between birth and death.

5.2. Cluster Dynamic Characteristics

Figure 11 summarises the statistics of all clusters that died within $t^* = 100$ for a Newtonian suspension at $Re_p = 0.57$ and $\phi = 31\%$ (about 12 000 clusters). Clusters are grouped by size: small (1–5 particles), medium (6–10), large (11–20) and super (21–∞), coloured yellow, blue, light purple and dark purple, respectively. Position, velocity, aspect ratio and radius of gyration are averaged over the lifetime of each cluster. The aspect ratio is obtained from principal-component analysis of the particle-coordinate covariance matrix.

Diagonal panels in Figure 11 are histograms; off-diagonal panels are scatter plots. The lifetime distribution is peaked below 0.5s and extends to 5s. Large clusters reside preferentially near the channel centre, whereas small ones are distributed over the entire gap with maxima close to the walls. Accordingly, large clusters move slowly (peak $\approx 0.003\mathrm{ms}^{-1}$), while small ones exhibit a broad velocity distribution with a peak close to the wall speed ($0.039\mathrm{ms}^{-1}$). Small clusters are also more elongated, reflecting chain-like agglomerates aligned with the compressional axis (cf. Figs.9 and10).

5.3. Cluster Lifetime

To understand the stability and evolution of clusters in shear flow, their lifetime distribution is analysed in detail. Figure 12 presents the survival function (complement of the cumulative distribution function) $P(T \geq t_{\mathrm{life}})$ for each size group. Large clusters exhibit the steepest slope ($\lambda = 1/\mu = 2.88$), implying the highest decay rate, whereas small clusters give the shallowest slope ($\lambda = 1.20$). The maximum lifetime observed for small clusters is 10.11s, whereas for large clusters it is only 3.46s. All survival curves are straight lines in semi-log coordinates, the hallmark of pure exponential decay, i.e. the probability of decay in any short interval is constant (memory-less process). When both axes are normalised by the mean lifetime $\langle t_{\mathrm{life}} \rangle$ (inset), the curves collapse onto a single master line, demonstrating that the decay mechanism is independent of cluster size.

To place the lifetime scale in physical context, we compare it with the micro-structural rearrangement time scales proposed by Andreotti, Forterre and Pouliquen (2013); Alghalibi et al. (2018). Assume a particle pressure P acting on the grains. Three microscopic time scales can be constructed by balancing P with drag forces:

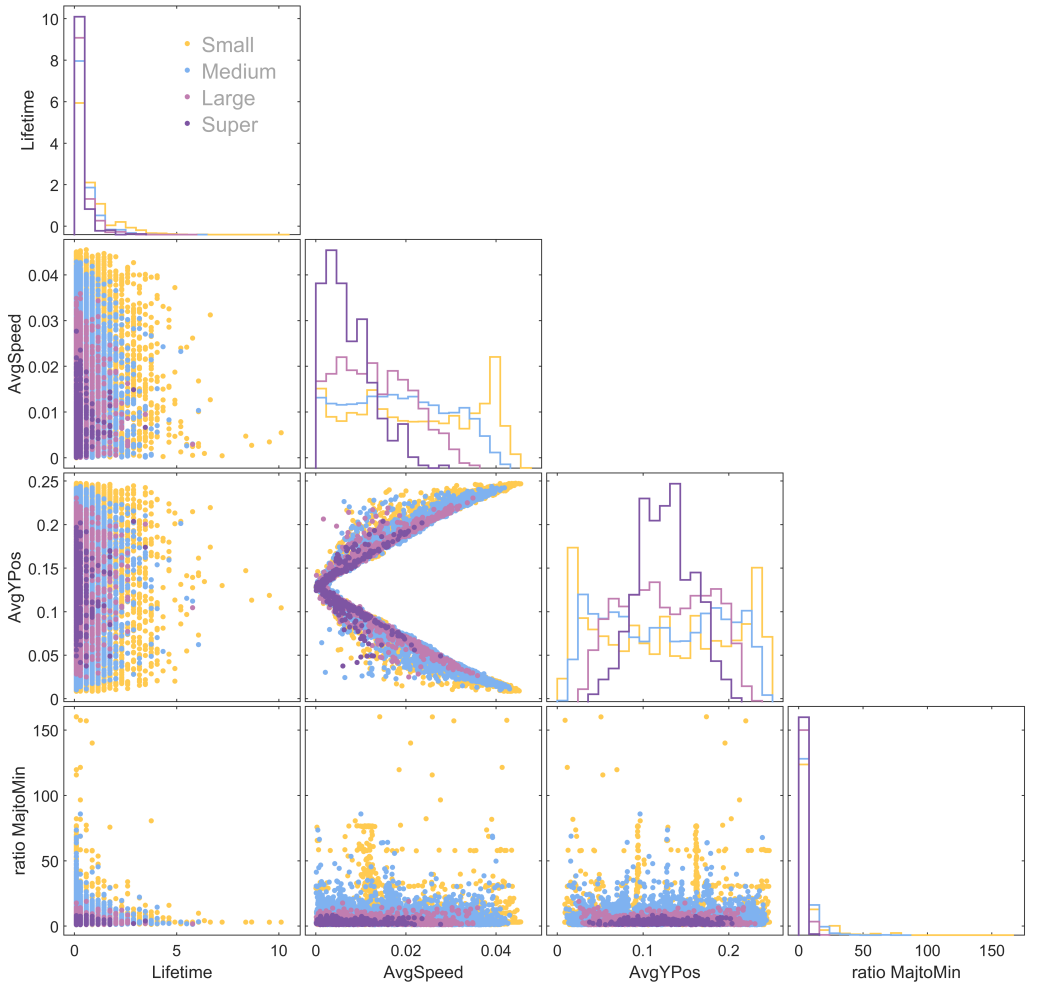

Figure 11: Scatter-matrix of cluster lifetime t_{life}, speed $\bar{v}$, centre position $\bar{y}$ and aspect ratio R_m for $Re_p = 0.57$, $\phi = 31\%$

$$
\begin{aligned}
t_1 &\sim \frac{d_p}{\sqrt{P/\rho_p}} \\
t_2 &\sim \frac{d_p}{\sqrt{P/(\rho_f C_d^{\text{st}})}} \qquad F_d = C_d d_p^2 \rho_f V^2 \\
t_3 &\sim \frac{d_p}{\sqrt{P/(\rho_f C_d^{\text{turb}})}}
\end{aligned}
\tag{28}
$$

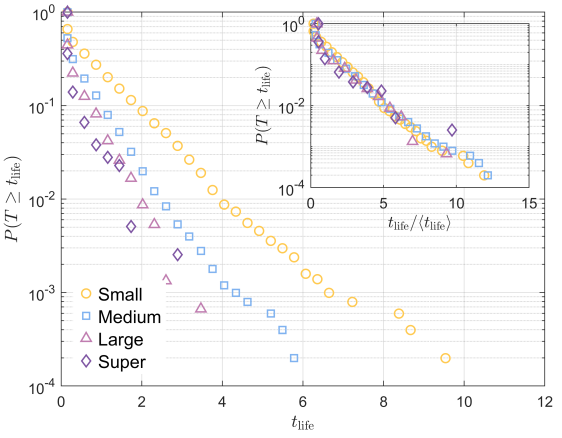

Figure 12: Survival function of cluster lifetimes

The corresponding non-dimensional parameters are $I = t_1\dot{\gamma}$, $J = t_2\dot{\gamma}$ and $J_I = t_3\dot{\gamma}$. The drag coefficient is taken from Tabuteau, Coussot and Bruyn (1985):

$$C_d = \begin{cases} \dfrac{24}{4Re_{p,\text{local}}} & 4Re_{p,\text{local}} < 1.4 \\ \dfrac{24/1.4^{0.375}}{(4Re_{p,\text{local}})^{0.625}} & 1.4 \leq 4Re_{p,\text{local}} \leq 500 \end{cases} \tag{29}$$

Ratios of the time scales,

$$\frac{t_1}{t_2} = \sqrt{\frac{\rho_p}{\rho_f}\frac{Re_{p,\text{local}}}{6}}, \qquad \frac{t_1}{t_3} = \left(\frac{\rho_p}{\rho_f}\right)^{1/2}(4Re_{p,\text{local}})^{5/16} \tag{30}$$

yield the regime diagram shown in Figure 13. All present simulations lie in the viscous-dominated region J, consistent with the constraint $Re_p < 1$.

The particle pressure P is evaluated from the trace of the averaged particle stress tensor:

$$P = \frac{1}{2}\text{tr}\langle\boldsymbol{\sigma}^p\rangle, \qquad \boldsymbol{\sigma}^p = -\frac{1}{V}\sum_{i\in V}\sum_{j>i}\boldsymbol{F}^c_{ij}\otimes\boldsymbol{r}_{ij} \tag{31}$$

giving $P \approx 3.73\times10^{-2}$Pa for the parameters of Figure 11. Inserting this value into Eq.(28) yields $t_1 \approx 5.3$s and $t_2 \approx 9$s, while the macroscopic shear time is $t = \dot{\gamma}^{-1} = 2.56$s. All these scales are one to two orders of magnitude

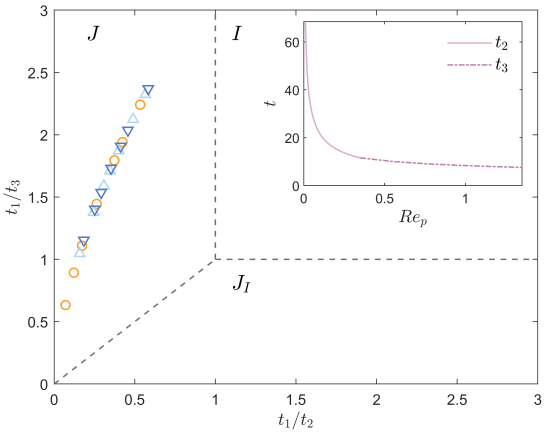

Figure 13: Regime diagram of sheared suspensions; inset: predicted time scales from Eq.(29)

larger than the observed cluster lifetimes (peak ≈ 0.02s, Figure 11). Hence clusters disintegrate long before any single-particle rearrangement mechanism becomes relevant. The discrepancy is attributed to (i) the theoretical expressions being derived for the grain scale, not for mesoscopic clusters, and (ii) the models being strictly valid only in the dense, pressure-dominated regime.

Clusters are therefore intrinsically non-equilibrium, transient structures. To demonstrate that they are nevertheless inertia-dominated on their own scale, we estimate an effective cluster Reynolds number. The internal shear rate is approximated by

$$\dot{\gamma}_{\text{cluster}} \approx \frac{v_{\text{cluster}}}{d_{\text{cluster}}} \tag{32}$$

with the cluster diameter taken as the radius of gyration

$$R_g = \sqrt{\frac{1}{N}\sum_{i=1}^{N} \|\boldsymbol{r}_i - \boldsymbol{r}_c\|^2} \tag{33}$$

Figure 14 shows that more than 80% of the clusters exhibit $Re_{p,\text{cluster}} = \rho_f v_{\text{cluster}} d_{\text{cluster}}/\mu_f > 1$, i.e. inertia dominates at the cluster scale even though the grain-scale flow is viscous-dominated. This scale separation is analogous to inertia-dominated eddies embedded in a viscous mean flow in classical turbulence. It also explains why the normalised survival functions of all size groups collapse onto a single exponential: the decay process is driven by the same inertia-controlled fluctuations.

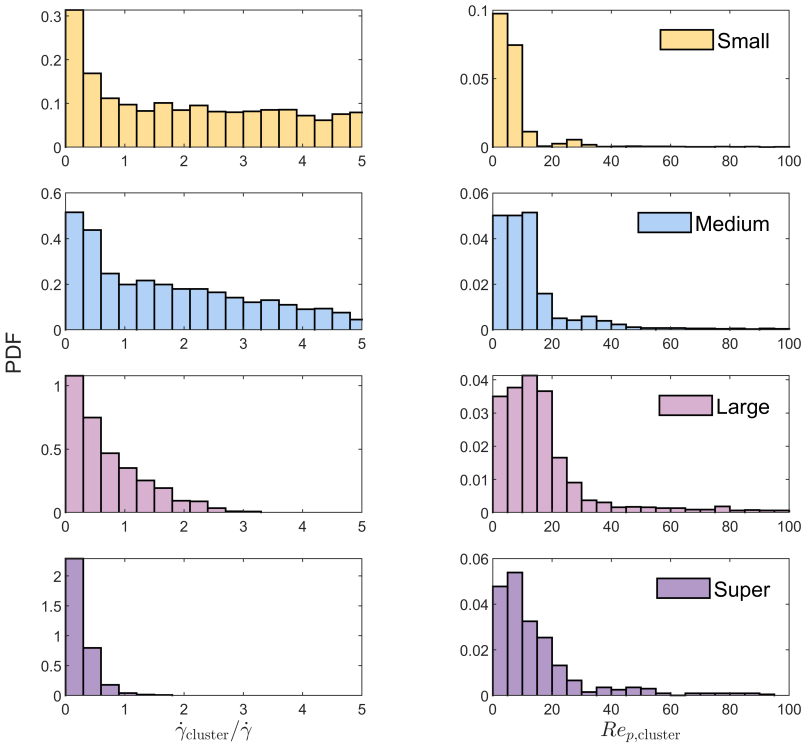

Figure 14: Histograms of cluster shear rate and cluster Reynolds number

6. Conclusion

This study employed a coupled LBM-IBM-DEM approach to systematically investigate the rheological behavior of suspensions with Newtonian, shear-thinning, and shear-thickening continuous phases under simple shear. Multi-scale analyses lead to the following principal conclusions:

1. At the macroscopic scale: The apparent viscosity exhibits shear-thickening behavior with increasing particle Reynolds number (Re_p) for all fluid models and rises markedly with solid volume fraction (ϕ). In the dilute regime ($\phi/\phi_c < 0.2$), the viscosity recovers the Einstein linear relation, while at higher concentrations, the data agree well with the Krieger-Dougherty model. Stress decomposition reveals that hydrodynamic forces govern the viscosity at low ϕ, whereas contact friction contributes more than 67% of the particle-induced stress at $\phi \approx 0.54$, underscoring a contact-dominated rheology at high concentrations.
2. At the microscopic scale: The radial distribution functions show that increasing concentration induces pronounced spatial correlations along the compressional axis ($\approx 45°$), which aligns with the orientation of active

contact force chains and corroborates the microstructural origin of the contact-dominated rheology observed macroscopically.

3. At the mesoscopic scale: A cluster-tracking algorithm, based on contact networks, revealed that cluster lifetimes follow an exponential distribution whose normalized survival curve is independent of size. This proves that cluster evolution is a memoryless process governed by universal stochastic dynamics. This finding demonstrates that the critical integration time step for the chain-to-arch transition in probability models is not merely a fitting parameter but can be scaled by a physically meaningful characteristic time—the average cluster lifetime. Scale analysis further shows that clusters are inertia-dominated transient structures at their own scale, disintegrating much faster than the microscopic rearrangement time, evidencing a clear scale separation.

A. Implementation of Non-Newtonian Fluids in LBM and Benchmark Test

The difference between non-Newtonian fluids and Newtonian fluids is that the kinematic viscosity is related to the shear rate. Taking a power-law fluid as an example, its dynamic viscosity μ is related to the shear rate $\dot{\gamma}$ as follows:

$$\mu = m\dot{\gamma}^{n-1}$$

where m is the fluid consistency coefficient and n is the flow behavior index. If expressed using kinematic viscosity ν, it differs by a factor of fluid density:

$$\nu = \frac{1}{\rho} m\dot{\gamma}^{n-1} \tag{A-1}$$

In LBM, kinematic viscosity is closely related to relaxation time:

$$\tau^* = \frac{\nu}{c_s^{*2}} + 0.5\Delta t \tag{A-2}$$

Therefore, the key to implementing non-Newtonian fluid simulation is to obtain the local shear rate for each lattice cell in the flow field, then calculate the corresponding relaxation time, and apply it to the collision process.

The shear rate of a fluid is the second invariant of the strain rate tensor $S_{\alpha\beta} = \frac{1}{2}(\frac{\partial u_\alpha}{\partial x_\beta} + \frac{\partial u_\beta}{\partial x_\alpha})$, expressed as:

$$\dot{\gamma} = \sqrt{2S_{\alpha\beta}S_{\alpha\beta}} \tag{A-3}$$

In LBM, the shear rate can be directly calculated from the distribution function (Artoli (2003); Krüger, Varnik and Raabe (2009); Chai, Shi, Guo and Rong (2011)), and its computational schemes include:

$$S_{\alpha\beta} = -(1-\frac{1}{\tau})\frac{1}{2\rho\nu}\sum_i f_i c_{i\alpha} c_{i\beta} \tag{A-4}$$

$$S_{\alpha\beta} = -\frac{1}{2\rho c_s^2 \tau}\sum_i \boldsymbol{e}_{i\alpha}\boldsymbol{e}_{i\beta}\left(f_i - f_i^{eq}\right) \tag{A-5}$$

$$S_{\alpha\beta} = -\frac{1}{2\rho c_s^2 \delta t}\sum_i c_{i\alpha} c_{i\beta}\sum_j \left(\left(\, M^{-1}SM \,\right)\right)_{ij}\left[\, f_j\left(\, x,t \,\right) - f_j^{eq}\left(\, x,t \,\right)\right] \tag{A-6}$$

$$S_{\alpha\beta} = -\frac{1}{2\rho c_s^2 \tau\left(\, x,t \,\right)\delta t}\sum_i \left(\, c_{i\alpha}c_{i\beta} - \frac{(\delta)_{\alpha\beta}}{3} c_i \cdot c_i \,\right)\left[\, f_i\left(\, x,t \,\right) - f_i^{eq}\left(\, x,t \,\right)\right] \tag{A-7}$$

Tests by Bisht and Patil (2020) show that the above schemes are consistent in calculating the fluid strain rate.

Unreasonable viscosity values can easily cause simulation divergence (e.g., inappropriate initialization). By limiting the range of relaxation time obtained from Eq. (A-2), divergence can be effectively suppressed. In this paper, the relaxation time $\tau \in [0.5+\epsilon, 2.0]$, where $\epsilon = 10^{-3}$.

The cavity flow is used as a benchmark test for the code. A schematic diagram of the cavity flow can be seen in Figure A1. The left, right, and bottom boundaries are all no-slip boundaries. The top boundary has a fixed characteristic velocity U_x in the x-direction. When the fluid follows the power-law model, the Reynolds number can be expressed as:

$$Re = \frac{\rho U^{2-n} L^n}{m} \tag{A-8}$$

Here, L is the characteristic length, which is the length of the square region, and the grid resolution is set to 256×256.

A test with a Reynolds number of 100 was conducted. The y-direction velocity component U_y at the cross-section $y = 0.5$ and the x-direction velocity component U_x at the cross-section $x = 0.5$ were extracted and plotted in Figure A2. The superscript * denotes the dimensionless form. The results show that the calculation for Newtonian fluid is

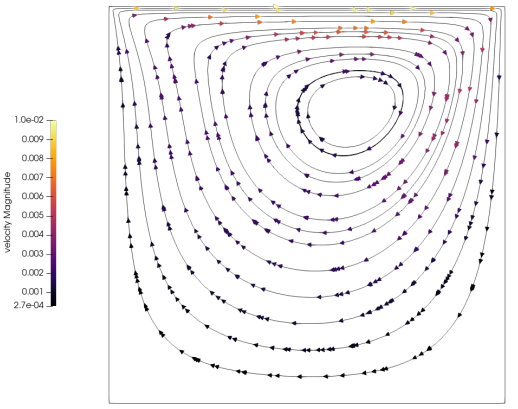

Figure A1: Schematic diagram of cavity flow. The streamlines in the figure are the calculation results for Newtonian fluid (n=1), and the arrow color represents the flow velocity.

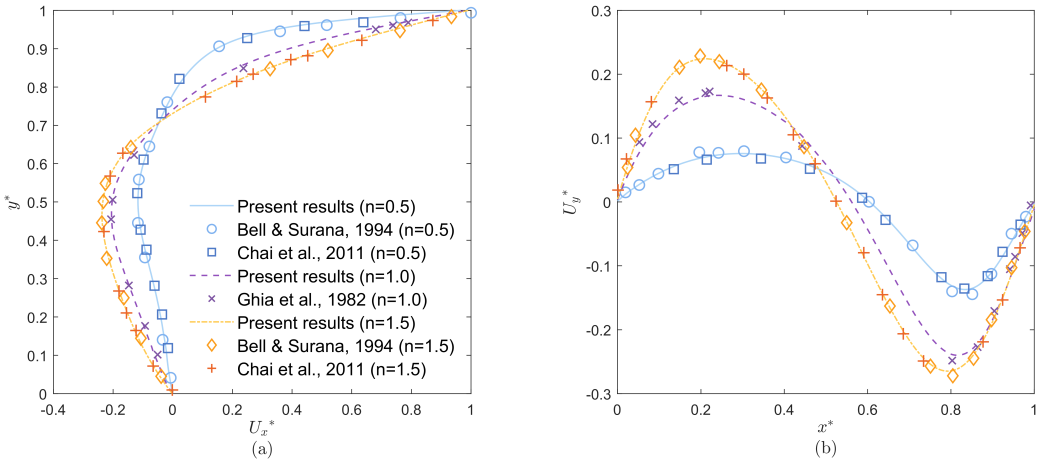

Figure A2: Velocity distribution of different power-law fluids in cavity flow

consistent with Ghia, Ghia and Shin (1982) (multigrid method). The non-Newtonian fluid results are consistent with those of Bell and Surana (1994) (NS equation solution) and Chai et al. (2011) (MRT collision model).

References

Alghalibi, D., Lashgari, I., Brandt, L., Hormozi, S., 2018. Interface-resolved simulations of particle suspensions in Newtonian, shear thinning and shear thickening carrier fluids. Journal of Fluid Mechanics 852, 329–357. doi:10.1017/jfm.2018.532.

Andreotti, B., Forterre, Y., Pouliquen, O., 2013. Granular Media: Between Fluid and Solid. Cambridge University Press.

Artoli, A.M.M., 2003. Mesoscopic Computational Haemodynamics. WageningenPonsen en Looijen. URL: https://dare.uva.nl/search?identifier=a2c3f64b-2998-438c-a67b-fc3487835749.

Batchelor, G.K., 1970. The stress system in a suspension of force-free particles. Journal of Fluid Mechanics 41, 545–570. URL: https://www.cambridge.org/core/journals/journal-of-fluid-mechanics/article/stress-system-in-a-suspension-of-forcefree-particles/3D8849DC49365A18E314C52E30A87ABC, doi:10.1017/S0022112070000745.

Bell, B.C., Surana, K.S., 1994. p-version least squares finite element formulation for two-dimensional, incompressible, non-newtonian isothermal and non-isothermal fluid flow. International Journal for Numerical Methods in Fluids 18, 127–162. URL: https://onlinelibrary.wiley.com/doi/abs/10.1002/fld.1650180202, doi:https://doi.org/10.1002/fld.1650180202, arXiv:https://onlinelibrary.wiley.com/doi/pdf/10.1002/fld.1650180202.

Bisht, M., Patil, D.V., 2020. Power-law fluid flow in driven enclosures with undulation using MRT-lattice Boltzmann method. Computers & Mathematics with Applications 79, 100–110. URL: https://www.sciencedirect.com/science/article/pii/S0898122117305540, doi:https://doi.org/10.1016/j.camwa.2017.09.006.

Boyer, F.m.c., Guazzelli, E., Pouliquen, O., 2011. Unifying suspension and granular rheology. Physical Review letters 107, 188301. URL: https://link.aps.org/doi/10.1103/PhysRevLett.107.188301, doi:10.1103/PhysRevLett.107.188301.

Chai, Z., Shi, B., Guo, Z., Rong, F., 2011. Multiple-relaxation-time lattice Boltzmann model for generalized Newtonian fluid flows. Journal of Non-Newtonian Fluid Mechanics 166, 332–342. URL: https://www.sciencedirect.com/science/article/pii/S0377025711000073, doi:https://doi.org/10.1016/j.jnnfm.2011.01.002.

Chateau, X., Ovarlez, G., Trung, K.L., 2010. Homogenization approach to the behavior of suspensions of noncolloidal particles in yield stress fluids. arXiv .

Eilers, H., 1941. Die Viskosität von Emulsionen hochviskoser Stoffe als Funktion der Konzentration. Kolloid-Zeitschrift 97, 313–321. URL: https://doi.org/10.1007/BF01503023, doi:10.1007/BF01503023.

Einstein, A., 1906. Eine neue Bestimmung der Moleküldimensionen. Annalen der Physik 324, 289–306. URL: https://onlinelibrary.wiley.com/doi/abs/10.1002/andp.19063240204, doi:10.1002/andp.19063240204. _eprint: https://onlinelibrary.wiley.com/doi/pdf/10.1002/andp.19063240204.

Einstein, A., 1911. Berichtigung zu meiner Arbeit: „Eine neue Bestimmung der Moleküldimensionen". Annalen der Physik 339, 591–592. URL: https://onlinelibrary.wiley.com/doi/abs/10.1002/andp.19113390313, doi:10.1002/andp.19113390313. _eprint: https://onlinelibrary.wiley.com/doi/pdf/10.1002/andp.19113390313.

Ergun, S., 1952. Fluid flow through packed columns. Chem. Eng. Prog 48, 89–94.

Ghia, U., Ghia, K.N., Shin, C.T., 1982. High-Re solutions for incompressible flow using the Navier-Stokes equations and a multigrid method. Journal of Computational Physics 48, 387–411. URL: https://www.sciencedirect.com/science/article/pii/0021999182900584, doi:https://doi.org/10.1016/0021-9991(82)90058-4.

Guazzelli, , Pouliquen, O., 2018. Rheology of dense granular suspensions. Journal of Fluid Mechanics 852, P1. URL: https://www.cambridge.org/core/journals/journal-of-fluid-mechanics/article/abs/rheology-of-dense-granular-suspensions/4F792CE372121D52299422BAEADCDE74, doi:10.1017/jfm.2018.548.

Herale, A.A., Pearce, P., Hewitt, D.R., 2025. Emergent clogging of continuum particle suspensions in constricted channels. Journal of Fluid Mechanics 1017, A24. doi:10.1017/jfm.2025.10468.

Jahanshahi Javaran, E., Rahnama, M., Jafari, S., 2014. Particulate flow simulation using lattice boltzmann method: A rheological study. Advanced Powder Technology 25, 1325–1333. URL: https://www.sciencedirect.com/science/article/pii/S0921883114001010, doi:https://doi.org/10.1016/j.apt.2014.03.012.

Kamali Zarch, M., Zhang, L., Haeri, S.M., He, J., 2025. Classic, modern, and physics-based rheological laws for geophysical granular flows in a landslide hazard chain. Earth-Science Reviews 269, 105204. URL: https://www.sciencedirect.com/science/article/pii/S0012825225001655, doi:https://doi.org/10.1016/j.earscirev.2025.105204.

Krieger, I.M., Dougherty, T.J., 1959. A Mechanism for Non-Newtonian Flow in Suspensions of Rigid Spheres. Transactions of The Society of Rheology 3, 137–152. URL: https://doi.org/10.1122/1.548848, doi:10.1122/1.548848. _eprint: https://pubs.aip.org/sor/jor/article-pdf/3/1/137/12574516/1_548848.pdf.

Krüger, T., Varnik, F., Raabe, D., 2009. Shear stress in lattice boltzmann simulations. Physical Review E 79, 046704. URL: https://link.aps.org/doi/10.1103/PhysRevE.79.046704, doi:10.1103/PhysRevE.79.046704.

Krüger, T., Kusumaatmaja, H., Kuzmin, A., Shardt, O., Silva, G., Viggen, E.M., 2016. The Lattice Boltzmann Method - Principles and Practice. doi:10.1007/978-3-319-44649-3.

Li, H., Zhao, Y., Li, J., Yin, H., Song, C., Hao, M., 2026. Cfd-dem investigation on continuous invasion behaviors of particles and evolution of pore clogging in porous media. Computers and Geotechnics 189, 107675. URL: https://www.sciencedirect.com/science/article/pii/S0266352X2500624X, doi:https://doi.org/10.1016/j.compgeo.2025.107675.

Li, Y.T. Guo, N. Yang, Z.X. Zhao, J.D. 2023. A fully resolved smoothed particle hydrodynamics-discrete element method study of the rheology of suspensions: The role of inertia and grain shape. Physics of Fluids 35, 083325. URL: https://doi.org/10.1063/5.0161344, doi:10.1063/5.0161344.

Mankoc, C., Garcimartín, A., Zuriguel, I., Maza, D., Pugnaloni, L.A., 2009. Role of vibrations in the jamming and unjamming of grains discharging from a silo. Physical Review E 80, 011309. URL: https://link.aps.org/doi/10.1103/PhysRevE.80.011309, doi:10.1103/PhysRevE.80.011309. publisher: American Physical Society.

Nabizadeh, M., Singh, A., Jamali, S., 2022. Structure and Dynamics of Force Clusters and Networks in Shear Thickening Suspensions. Physical Review Letters 129, 068001. URL: https://link.aps.org/doi/10.1103/PhysRevLett.129.068001, doi:10.1103/PhysRevLett.129.068001. publisher: American Physical Society.

Picano, F., Breugem, W.P., Mitra, D., Brandt, L., 2012. Shear thickening in non-brownian suspensions: An excluded volume effect. Physical Review Letters 111, 098302.

Qiu, Z., Xiao, Q., 2025. Exploring the 'fast is slow' effect in particle suspension clogging: Liquid driving and random walk models. Powder Technology 454, 120690. URL: https://www.sciencedirect.com/science/article/pii/S0032591025000853, doi:https://doi.org/10.1016/j.powtec.2025.120690.

Srinivasan, S., Akker, H.E.A.V.d., Shardt, O., 2021. Numerical simulations of dense granular suspensions in laminar flow under constant and varying shear rates. Computers & Fluids 230, 105115. URL: https://www.sciencedirect.com/science/article/pii/S0045793021002632, doi:https://doi.org/10.1016/j.compfluid.2021.105115.

Srinivasan, S., Van den Akker, H.E., Shardt, O., 2020. Shear thickening and history-dependent rheology of monodisperse suspensions with finite inertia via an immersed boundary lattice boltzmann method. International Journal of Multiphase Flow 125, 103205. URL: https://www.sciencedirect.com/science/article/pii/S0301932219306081, doi:https://doi.org/10.1016/j.ijmultiphaseflow.2019.103205.

Tabuteau, H., Coussot, P., Bruyn, J., 1985. Drag force on a sphere in steady motion through a yield-stress fluid. J. Fluid Mech. Beaulne and Mitsoulis J. Non-Newtonian Fluid Mech 158, 219–244. doi:10.1122/1.2401614.

Thøgersen, K., Dabrowski, M., Malthe-Sørenssen, A., 2016. Transient cluster formation in sheared non-Brownian suspensions. Physical Review E 93, 022611. URL: https://link.aps.org/doi/10.1103/PhysRevE.93.022611, doi:10.1103/PhysRevE.93.022611. publisher: American Physical Society.

To, K., Lai, P.Y., Pak, H.K., 2001. Jamming of granular flow in a two-dimensional hopper. Physical Review letters 86, 71–74. URL: https://link.aps.org/doi/10.1103/PhysRevLett.86.71, doi:10.1103/PhysRevLett.86.71.

Vand, V., 1948. Viscosity of Solutions and Suspensions. I. Theory. The Journal of Physical and Colloid Chemistry 52, 277–299. URL: https://doi.org/10.1021/j150458a001, doi:10.1021/j150458a001. publisher: American Chemical Society.

Yang, X., Li, S., Li, G., Li, R., Kadhim Kadhim, M.M., Li, H., Duan, M., Li, Z., 2024. Visualization experiment on dynamic migration and sealing mechanism of irregular materials in rough fractures. Geoenergy Science and Engineering 242, 213251. URL: https://www.sciencedirect.com/science/article/pii/S2949891024006213, doi:https://doi.org/10.1016/j.geoen.2024.213251.

Zhang, S., Zeng, Z., Yuan, H., Li, Z., Wang, Y., 2024. Precursory arch-like structures explain the clogging probability in a granular hopper flow. Communications Physics 7, 202. URL: https://doi.org/10.1038/s42005-024-01694-7, doi:10.1038/s42005-024-01694-7.

Zuriguel, I., Pugnaloni, L.A., Garcimartín, A., Maza, D., 2003. Jamming during the discharge of grains from a silo described as a percolating transition. Physical Review E 68, 030301. URL: https://link.aps.org/doi/10.1103/PhysRevE.68.030301, doi:10.1103/PhysRevE.68.030301. publisher: American Physical Society.